










Doppler optical frequency domain reflectometry for remote fiber sensing

MAX KOEPPEL,^{1,2,6}  ABHINAV SHARMA,^{3,4}  JASPER PODSCHUS,¹  SANJU SUNDARAMHALINGAM,³ NICOLAS Y. JOLY,^{2,3,4,5}  SHANGRAN XIE,^{3,7}  PHILIP ST. J. RUSSELL,^{3,4}  AND BERNHARD SCHMAUSS^{1,2,3} 

¹*Institute of Microwaves and Photonics, Friedrich-Alexander University, Erlangen, Germany*

²*Graduate School in Advanced Optical Technologies, Erlangen, Germany*

³*Max Planck Institute for the Science of Light, Erlangen, Germany*

⁴*Department of Physics, Friedrich-Alexander University, Erlangen, Germany*

⁵*Interdisciplinary Center for Nanostructured Films, Erlangen, Germany*

⁶*max.koeppel@fau.de*

⁷*shangran.xie@mpl.mpg.de*

Abstract: Coherent optical frequency domain reflectometry has been widely used to locate static reflectors with high spatial resolution. Here, we present a new type of Doppler optical frequency domain reflectometry that offers simultaneous measurement of the position and speed of moving objects. The system is exploited to track optically levitated “flying” particles inside a hollow-core photonic crystal fiber. As an example, we demonstrate distributed temperature sensing with sub-mm-scale spatial resolution and a standard deviation of $\sim 10^\circ\text{C}$ up to 200°C .

© 2021 Optical Society of America under the terms of the [OSA Open Access Publishing Agreement](#)

1. Introduction

Coherent optical frequency domain reflectometry (COFDR) was originally proposed as an alternative to optical time domain reflectometry (OTDR) [1–3]. Since it offers a spatial resolution several orders of magnitude better than OTDR, it also allows the analysis of small-scale components and integrated optical waveguides [4–7]. The high resolution and sensitivity is useful in many different sensing applications, for example, distributed temperature or strain sensing based on Rayleigh scattering fingerprints [8–10].

In many sensing situations there is also a great need for dynamic measurements. Although COFDR systems for detecting vibrations or acoustic signals have been reported [11, 12], they have not yet been extended to dynamic measurements of moving targets. Here, we report for the first time a Doppler COFDR system in which the instantaneous position and speed of moving objects are measured with μm -scale spatial resolution and speed accuracy in the $\mu\text{m}/\text{s}$ -range. Using a custom-built dynamic OFDR system, the position and speed of optically levitated flying particles in a hollow-core photonic crystal fiber (HC-PCF) were continuously monitored, permitting realization of a versatile distributed temperature sensor with high spatial resolution.

2. Principle of Doppler OFDR

Figure 1 shows a sketch of the Doppler COFDR system, which is based on a Mach-Zehnder topology. Analogously with radio-frequency-modulated radar systems, the laser frequency was linearly swept so as to remove the distance ambiguity inherent to conventional interferometers. The laser output was split up into a reference and a measurement arm incorporating the reflecting target. First, assuming a steady target with reflectivity R , the time varying signal (after filtering

out the DC and sum-frequency components) collected by a square-law detector can be written as:

$$\begin{aligned} I_{AC}(t) &\propto \text{Re} \left\{ \sqrt{R} s(t) s^*(t - \tau) \right\} \\ &= \text{Re} \left\{ \sqrt{R} \exp(j2\pi(f_0\tau + k\tau t - k\tau^2/2)) \right\} = \text{Re}\{b(t)\}, \end{aligned} \quad (1)$$

where $s(t) = \exp(j(2\pi f_0 t + \pi k t^2))$ is the normalized linearly chirped optical field, with start frequency f_0 and sweep rate $k = B/T$, covering frequency bandwidth B over time T . The time delay between the two arms $\tau = 2z_0/c$ is determined by the target position z_0 relative to the reference path length and the speed of light c . For the sake of simplicity, we assume the polarization states to be perfectly aligned throughout, which can be achieved by including a polarization controller in the reference path.

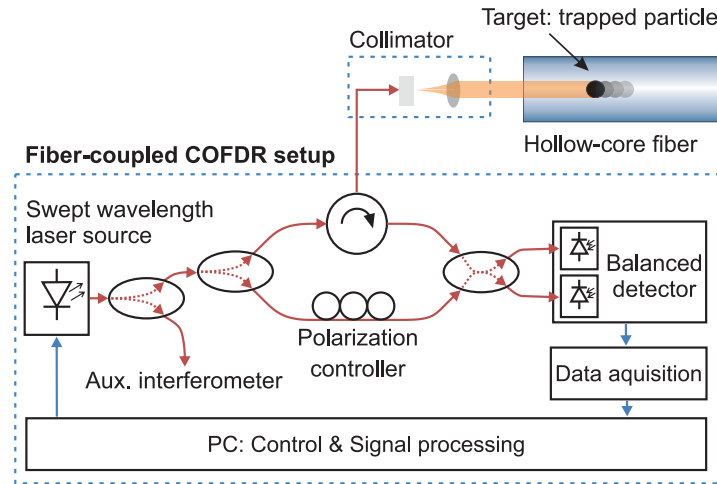


Fig. 1. COFDR setup in Mach-Zehnder topology.

Frequency analysis of Eq. (1) yields a beat frequency:

$$f_b = \frac{1}{2\pi} \frac{d}{dt} \arg[b(t)] = k\tau. \quad (2)$$

For static objects, assuming negligible dispersion over the sweep bandwidth, the distance can be readily calculated from the beat frequency:

$$z_0 = c \frac{\tau}{2} = c \frac{f_b}{2k}. \quad (3)$$

The two-point spatial resolution of COFDR is determined by the target main lobe width of the Fourier transform [4]:

$$\Delta z = \frac{c}{2B}. \quad (4)$$

Note that the exact target position can be determined much more precisely by approximating the peak with a second-order polynomial and calculating its maximum position. Using a conventional COFDR system, we have previously demonstrated localization of optically trapped particles with a precision of $\sim 2 \mu\text{m}$, corresponding to $\sim 1/15$ of the two-point resolution [13].

In order to analyze the effects of (uniformly) moving targets, τ in Eq. (1) is replaced by:

$$\tau(t) = \frac{2z(t)}{c} = \frac{2(z_0 + v_0 t)}{c}, \quad (5)$$

where v_0 is the target speed. Since v_0 is much smaller than c in our application, any relativistic effects can be neglected and the beat signal becomes

$$b(t) = \exp \left\{ j2\pi \left[\left(\frac{2kv_0}{c} - \frac{2kv_0^2}{c^2} \right) t^2 + \left(\frac{2f_0 v_0}{c} + \frac{2kz_0}{c} - \frac{4kv_0 z_0}{c^2} \right) t + \frac{2f_0 z_0}{c} - \frac{2kz_0^2}{c^2} \right] \right\}, \quad (6)$$

giving rise to the beat frequency:

$$f_{\text{beat}}(t) = \underbrace{\frac{2f_0 v_0}{c}}_{\text{I}} + \underbrace{\frac{2kz_0}{c}}_{\text{II}} + \underbrace{\left(\frac{4kv_0}{c} - \frac{4kv_0^2}{c^2} \right) t}_{\text{III}} - \underbrace{\frac{4kv_0 z_0}{c^2}}_{\text{IV}} \approx \frac{2f_0 v_0}{c} + \frac{2kz_0}{c} + \underbrace{\frac{4kv_0}{c}}_{\text{V}} t. \quad (7)$$

In Eq. (7) the first term (I) describes a frequency shift caused by the Doppler effect, the second term (II) is the beat frequency due to the static distance, the third term (III) resembles a quadratic phase chirp caused by the movement of the target and the last term (IV) depends on both the speed and position of the target. In most applications, the terms proportional to c^{-2} are tiny and therefore can be neglected. Equation (7) indicates that the beat frequency not only depends on the target distance but also on the target speed (i.e. range-Doppler coupling effect). The time dependent chirp term (V) in Eq. (7) will cause the target peak to blur in the reflection profile, which gets broader as the target moves faster. Thus, this chirp will reduce the peak height and the detection sensitivity for moving targets. Therefore, this needs to be compensated if the position and speed of the target are to be accurately measured.

A phase-gradient autofocus algorithm, initially proposed for synthetic aperture radar images [14], was used to refocus the target peak. First, coarse peak detection and windowing of the reflection profile were applied around the peak of interest. The window width was set wide enough to cover the full peak energy and yet small enough to exclude noise. Although this algorithm can be applied iteratively, a fixed window size and a single iteration were sufficient for our application. The windowed section of the reflection profile containing the peak of interest was shifted to the origin and the phase error derivative was determined using the relation given in [14,15]. The phase errors were then determined by numerical integration and any linear slope was compensated for, since this would cause a target position error. Eventually, the blur was mitigated by multiplying the windowed peak spectrum with the conjugate phase term and shifting back the peak to its original position in the reflection profile. Naturally, this correction not only compensates the chirp term (V) but also removes the phase distortions remaining after imperfect sweep nonlinearity correction (see Appendix A.1). Figure 2 depicts the reflection profiles (up and down sweep) of a moving target (2- μm -diameter silica particle trapped and propelled inside HC-PCF with a moving speed of ~ 30.4 mm/s) before and after applying the autofocus algorithm. It can be seen that peak broadening due to the phase chirp effect can be effectively suppressed by re-focusing.

Once the chirp term is compensated, two consecutive independent measurements are combined to determine the position and speed of the target. Figure 3 depicts the impact of the Doppler frequency shift and the time delay related to the target distance on the measured beat frequency.

Assuming ideal up and down sweeps with the same absolute sweep rate $|k|$ (but opposite signs) for both measurements, the target position and speed can be calculated from the beat frequencies

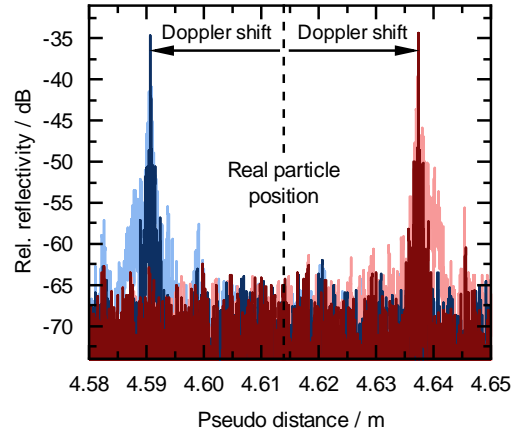


Fig. 2. Calculated reflection profile for the up (red) and down (blue) ramp for a propelled 2- μm -diameter silica particle through the HC-PCF with (saturated colors) and without (faint colors) refocusing.

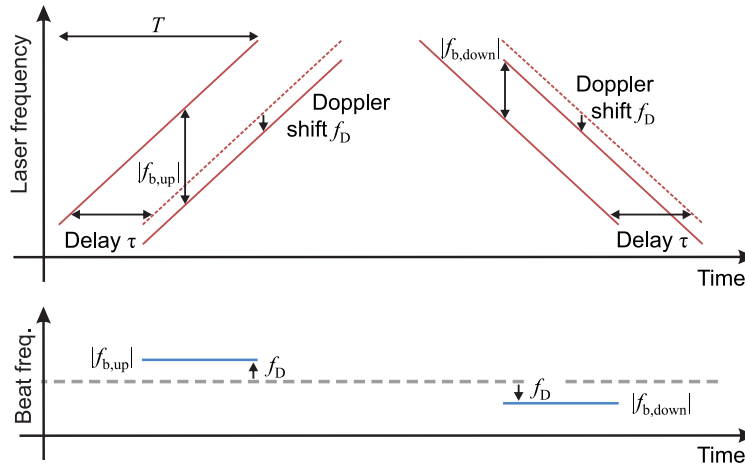


Fig. 3. Influence of Doppler frequency shift on the measured beat frequency caused by a moving target.

$|f_{b,up}|$ and $|f_{b,down}|$:

$$z_0 = \frac{c}{4|k|} (|f_{b,up}| + |f_{b,down}|), \quad (8)$$

$$v_0 = \frac{c}{4f_0} (|f_{b,up}| - |f_{b,down}|), \quad (9)$$

where movement of the target between the two measurements is neglected. Accounting for different sweep rates k_1 , k_2 and durations T_1 , T_2 and a measurement time delay Δt between the up and down ramps (starting at f_{01} and f_{02} respectively), the position and speed can be retrieved as (see Appendix A.2 for the derivation):

$$z_0 = \frac{[T_1 k_1 (\Delta_- f_b - \Delta_+ f_b) + \Delta_- f_b \Delta f_0 - \Delta_+ f_b (f_{01} + f_{02}) - (\Delta t + T_2) (\Delta_+ f_b + \Delta_- f_b) k_2] c}{4[(T_1 - T_2 - \Delta t) k_1 k_2 - f_{01} k_2 - f_{02} k_1]}, \quad (10)$$

$$v_0 = \frac{[(\Delta_+f_b - \Delta_-f_b)k_1 + k_2(\Delta_+f_b + \Delta_-f_b)]c}{4\{[(T_1 - T_2 - \Delta t)k_2 - f_{02}]k_1 + f_{01}k_2\}}, \quad (11)$$

where $\Delta f_0 = f_{01} - f_{02}$, $\Delta_+f_b = |f_{b,up}| + |f_{b,down}|$ and $\Delta_-f_b = |f_{b,up}| - |f_{b,down}|$.

Note that in contrast to conventional Doppler velocimetry based on fixed-wavelength laser [16], the system can measure the instantaneous absolute position of the moving objects and is not subject to integration error over time.

3. Tracking of optically trapped and propelled particles in HC-PCF

The Doppler COFDR system was used to track optically trapped particles in HC-PCF. Flying particle sensors in HC-PCF have inherent advantages such as galvanic isolation and coverage of long distances, while additionally offering reconfigurability, improved spatial resolution and multi-parameter sensing [17]. The experimental setup is shown in Fig. 4. The 1030 nm trapping laser emitted ~ 200 fs pulses at a repetition rate of 70 MHz. The average total trapping power was ~ 2 W. The use of a pulsed laser is necessary to suppress inter-modal beating between fundamental and higher order core modes [18]. The measured modal walk-off distance is ~ 20 cm (see Appendix A.3). The high repetition frequency of the pulse train ensures that gravity-related particle displacement between pulses is negligible. The COFDR probe beam at 1550 nm wavelength was coupled into the beam path using a dichroic mirror. The power ratio of the trapping beams was set using a motorized half-wave plate to adjust the polarization state of the trapping laser in front of a polarizing beam-splitter. We used a commercially available swept-wavelength laser source (Luna Phoenix 1400 PM) with a maximum tuning range of 50 nm around a central wavelength of 1540 nm at a maximum tuning rate of 2000 nm/s (i.e. a sweep rate of approx. 2.5×10^{14} Hz s^{-1}). The inset in Fig. 4 shows a scanning electron micrograph of the single-ring HC-PCF. It has a core diameter of ~ 30 μm and can guide both the trapping beam and the COFDR probe beam with low loss. The microparticles in a suspension were sprayed into a trapping chamber in front of the end face of the HC-PCF, where they were trapped by two counter-propagating laser beams and then propelled into the hollow core by adjusting the power ratio of the trapping beams. The trapping of single (as opposed to multiple) particles in the hollow core was verified by monitoring the scattered light from the side of the fiber using an infrared viewer.

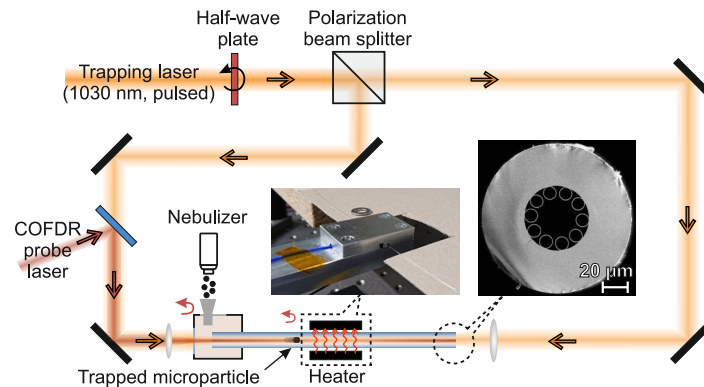


Fig. 4. Experimental setup for tracking optically trapped microparticles in a HC-PCF using Doppler COFDR and the configuration for remote temperature sensing.

We first tested the achievable precision of position measurement for silica microparticles with different sizes at the maximum sweep rate. In each configuration, a series of 100 repeat measurements was conducted for which the measured standard deviation is plotted in Fig. 5(a) as a function of sweep bandwidth. It can be seen that the measurement data fits excellently with the

inverse proportionality suggested in Eq. (4). Since the sweep bandwidth is directly linked to the measurement duration, it is possible to balance position precision against measurement rate (see upper axis). Furthermore, the achievable precision is related to the signal-to-noise ratio (SNR) of the target reflection peak, which is higher for larger particles and greater sweep bandwidths. In practice, the maximum measurement rate will be reached once the SNR of the target peak is too low to be detected reliably. For highly reflective targets, it is limited by the minimum sweep duration of the tunable laser source. With the laser used, measurement rates up to approximately 250 Hz could be achieved. At the cost of reduced precision, measurement rates in the kHz range are feasible using commercially available sources.

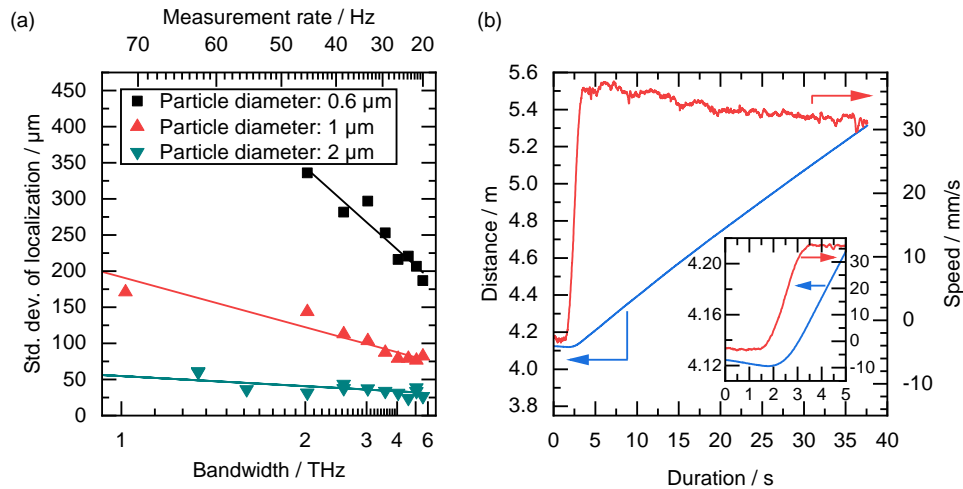


Fig. 5. (a) Measured positional precision versus sweep bandwidth for different particle sizes. The solid lines are fits using inverse proportionality. (b) Instantaneous position (blue) and speed (red) of a tracked 2- μm -diameter silica particle in HC-PCF. The inset is a zoom into the first 5 s, during which the particle accelerates.

Figure 5(b) shows the tracking of a moving silica particle with 2 μm diameter that is propelled along the fiber for around 38 s (see Table 1 for detailed COFDR parameters). We tentatively attribute the small-scale speed variations to fluctuations in trapping laser power (see Appendix A.4) that could be reduced using active power stabilization. The speed fluctuations may be also partly caused by fiber non-uniformities or static charges on the core wall, while the overall exponential speed reduction is due to fiber attenuation. The accuracy of the speed measurement (a few tens of $\mu\text{m}/\text{s}$) was assessed using a mirror on a linear stage moving at a known speed (see Appendix A.5). Note that both positive (forward) and negative (backward) particle speeds can be measured by the system. The maximum target speed that can be measured is limited by the Nyquist sampling theorem for highly reflective targets and by the SNR for weakly reflecting targets.

Table 1. COFDR measurement parameters

Wavelength sweep range	1535 nm – 1545 nm
Probe laser power (at HC-PCF end face)	5.4 mW
Sweep rate	2000 nm/s
Measurement update rate	62.4 Hz
ADC sampling frequency	20.8 MS/s
Maximum measurement range	6.2 m (in air)
Two-point resolution	120 μm (in air)

4. Remote temperature sensing

Next, we used flying particles in HC-PCF in combination with Doppler COFDR to build a distributed temperature sensor. In the experiment, silica particles of diameter 2 μm were once again propelled by adjusting the power ratio of the counter-propagating trapping beams. The terminal velocity of the particle is determined by the balance between the scattering force F_{opt} and the Stokes drag force F_{drag} [17]:

$$F_{\text{opt}} = F_{\text{drag}} = 6\pi K a_p \mu(T) v, \quad (12)$$

where $\mu(T)$ is the viscosity of air, K is a wall correction factor accounting for the turbulence in the narrow core [19], a_p the particle radius and v is the particle speed. For constant optical force F_{opt} the temperature-dependent particle velocity is given by:

$$v(T) = \frac{F_{\text{opt}}}{6\pi K a_p \mu(T)}, \quad (13)$$

where the temperature dependence of the viscosity can be modelled using the Sutherland formula [20]:

$$\mu(T) = \mu_{\text{ref}} \left(\frac{T}{T_{\text{ref}}} \right)^{3/2} \frac{T_{\text{ref}} + S}{T + S}, \quad (14)$$

where S is the Sutherland constant (111 K for air [21]) and μ_{ref} is the viscosity at the reference temperature T_{ref} .

A 2-meter-long single-ring HC-PCF was used in the measurement. As shown in Fig. 4, a section of 2.5 cm was fed through an aluminum block and heated to temperatures up to 200 $^{\circ}\text{C}$ while the rest of the fiber was kept at room temperature. The temperature of the metal block was measured using an embedded temperature sensor with an accuracy of 2.5 K (IEC 584, type K, class 2). The particle was propelled through a ~ 50 cm long fiber section containing the heater while its absolute position and speed were measured. The COFDR parameters are summarized in Table 1.

So as to mitigate the effects of any overall speed drift with time, all the experimental measurements of particle speed were normalized to the average speed in a reference fiber section held at room temperature (see Fig. 6(a)). The estimated spatial resolution for the COFDR configuration was 120 μm , corresponding to the ultimate theoretical spatial resolution, while the mean particle speed in the reference section was measured to be 29.1 mm/s, yielding position and speed data at intervals of 0.47 mm on average. Since this corresponds to the spatial sampling distance, it sets the upper bound for the spatial resolution of the temperature sensor. By further adjusting the particle speed it is possible to balance the spatial resolution and the time required to propel the particle along the fiber length. Note that the steep temperature gradients at the edges of the heater cause thermal creep flow of air within the hollow core (related to Knudsen pumps [22]), leading to visible undershoots and fluctuations in speed in the vicinity of these

points. Based on Eq. (13) and (14), a speed reduction of $\sim 20\%$ for a temperature increase of 100 K starting from room temperature is expected. This in good agreement with the experimental results. The observed decrease in speed over distance within the heated section we attribute tentatively to the thermal creep effect, pending a full investigation.

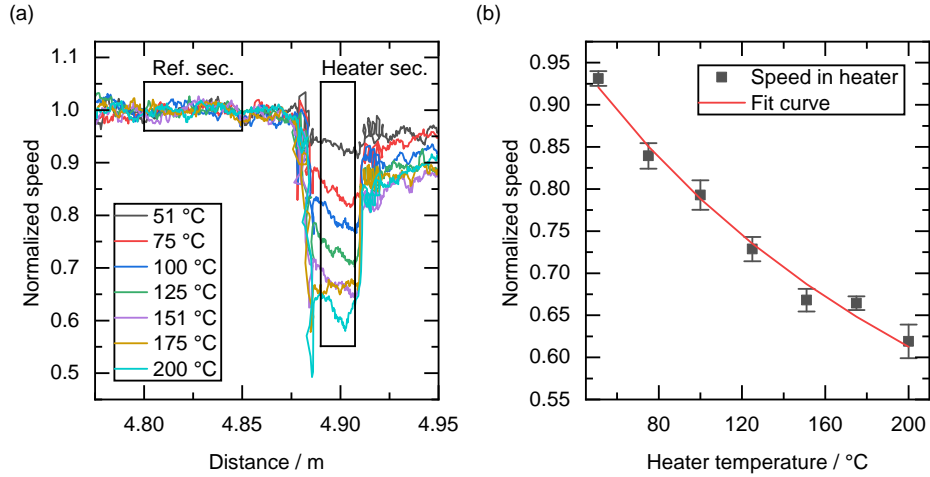


Fig. 6. (a) Measured particle speed versus location for different heater temperatures.(b) Measured average particle speed in the heater section (squares) and curve fit using Eq. (15) (red line).

To calibrate the sensor, the average particle speed in the heater section was first measured at seven different metal block temperatures (Fig. 6). The error bars in Fig. 6(b) are given by the standard deviation of the speed fluctuations over distance within the heater section (see Fig. 6(a)). Combining Eq. (13) and (14), the temperature dependence of particle speed can be written as:

$$v(T) = C \cdot \frac{T(\alpha_T T + \alpha_0) + S}{[T(\alpha_T T + \alpha_0)]^{3/2}}, \quad (15)$$

where the scaling factor $\alpha(T) = \alpha_T T + \alpha_0$ was used to relate the actual temperature of the air in the hollow core to the metal block temperature, read from the heater. A least-squares fit of the data-points to Eq. (15) yields $C = 10.72 \text{ m s}^{-1} \text{ K}^{1/2}$, $\alpha_0 = 0.4902$, $\alpha_T = 1.058 \times 10^{-3} \text{ K}^{-1}$ with $S = 111 \text{ K}$ [21]. Equation (15) was then used to retrieve the temperature for a series of measurements taken during the heating and subsequent cooling of the heater. The calculated temperatures, together with the deviations in the measured metal temperatures, are shown in Fig. 7(a) and 7(b). The calculated standard deviation for temperatures up to 100 °C was 4.94 °C whereas the overall standard deviation was $\sim 10.3^\circ\text{C}$. The increased temperature deviation at higher temperatures in Fig. 7(b) is partly caused by the reduced temperature sensitivity, i.e. the reduced slope of $v(T)$ -fit curve (see Fig. 6(b)). An improved approach to calibrating the temperature from the particle speed is expected to further increase the resolution of the temperature measurement.

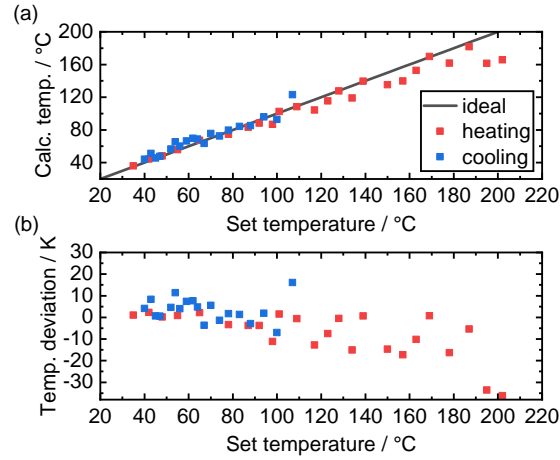


Fig. 7. (a) Calculated and set temperatures for measurements during heating and cooling of the heater. (b) Deviation between calculated temperature and set temperature.

5. Conclusion

These proof-of-principle experiments demonstrate that a Doppler OFDR system can track the instantaneous absolute position and speed of moving objects with high accuracy. Such a system can be used to probe the motion dynamics of macroscopic objects with micrometer spatial resolution. It can also be used to probe the viscoelasticity of the gases or liquids in the hollow-core of a HC-PCF. The integration of Doppler OFDR with particle guidance in HC-PCF opens up novel possibilities for flying particle sensors capable of measuring multiple physical quantities with high-spatial resolution. Since the COFDR system can also track the positions of multiple particles [13], it may be exploited to investigate the dynamics of levitated particles or bound particle arrays in HC-PCF [18].

Appendix

A.1. Sweep linearization of COFDR

Even for highly optimized sweeping lasers, there always remains a residual deviation from a perfect frequency ramp, resulting from environmental influences or the internal sweep feedback mechanisms. It is intuitively clear that any deviation from an ideal sweep will lead to a time-varying beat signal and therefore distort the reflection profile. As a result, the localization precision will be reduced or, in the case of oscillating deviations, side-lobes will occur and corrupt the reflection profile.

To analyze this effect, the ideal laser sweep signal is extended with a phase error function $\phi_e(t)$:

$$s(t) = \exp(j2\pi(f_0t + kt^2/2) + j2\pi\phi_e(t)), \quad (16)$$

where $\phi_e(t)$ consists of a deterministic (but unknown) error term $\phi_{nl}(t)$ caused by the sweep nonlinearity and a stochastic process $\phi_{pn}(t)$ used to model the laser phase noise:

$$\phi_e(t) = \phi_{nl}(t) + \phi_{pn}(t). \quad (17)$$

This yields the beat signal in complex notation after down-mixing, low-pass filtering and scaling (assuming an interferometer delay τ and neglecting any losses):

$$b_e(t, \tau) = \sqrt{R} \exp(j2\pi(kt\tau + f_0\tau - kt^2/2)) \cdot \exp(j2\pi\Delta\phi_e(t, \tau)), \quad (18)$$

where $\Delta\phi_e(t, \tau) = \Delta\phi_{nl}(t, \tau) + \Delta\phi_{pn}(t, \tau)$ with $\Delta\phi_x(t, \tau) = \phi_x(t) - \phi_x(t - \tau)$. For a semiconductor laser, $\phi_{pn}(t)$ is normally modelled as a Wiener process, meaning that $\Delta\phi_{pn}$ is a stationary Gaussian random process and therefore only depends on τ . For delays much smaller than the laser coherence time τ_c , $\Delta\phi_{pn} \sim 0$ holds and the impact of the laser phase noise can be neglected.

To correct the effect of a deterministic phase error term $\phi_{nl}(t)$, an auxiliary interferometer was used to interpolate the actual laser frequency for each sample. An absolute wavelength reference (an absorption cell) is available from trigger signals provided by the laser source at predefined wavelengths. The measurement interferometer signal was then resampled at equidistant source frequencies.

Figure 8(a) plots a section of the auxiliary interferometer signal (after subtracting a slowly varying DC component). First, the exact zero crossings (red markers) were determined by linear interpolation between data-points on either side of the sign changes. In a second step, the mean distance between zero crossings with rising and falling slopes was calculated (blue markers) and used for interpolation. Figure 8(b) shows auxiliary signal period length (resembling equidistant frequency intervals) determined from the markers for a laser sweep from 1535 nm to 1545 nm in ~ 5 ms sampled at 20.8 MS/s. The reference delay τ_{ref} was chosen small enough to allow direct monitoring of the laser frequency. Even though a longer delay leads to a smaller free spectral range in the auxiliary interferometer, and thus a finer “sampling” of the laser frequency, the limit for τ_{ref} is the maximum sampling frequency since oversampling is required to precisely determine the positions of the zero crossings. Table 2 lists the parameters of the auxiliary interferometer in the COFDR system. The delay fiber in the auxiliary interferometer was placed in a styrodur box so as to shield it from environmental influences. Furthermore, polarization maintaining fibers were used in the auxiliary interferometer to avoid polarization-related drift.

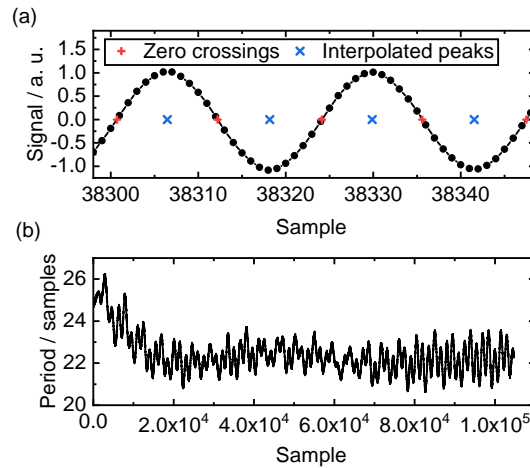


Fig. 8. Working principle of the auxiliary-based resampling technique. (a) Section of the auxiliary interferometer signal. (b) Period length of the beat signal during the sweep.

The correction term extracted from the auxiliary interferometer with delay τ_{ref} is given by:

$$c_a(t) = \exp(-j2\pi\Delta\phi_{nl}(t, \tau_{ref})) = \exp(-j2\pi(\phi_{nl}(t) - \phi_{nl}(t - \tau_{ref}))), \quad (19)$$

where we assume $\tau_{ref}, \tau_{meas} \ll \tau_c$ so that the influence of laser phase noise is neglected. Using this term to correct the measurement signal $b_e(t, \tau_{meas})$ we obtain:

$$b_{corr}(t, \tau_{meas}) = c_a(t) \cdot b_e(t, \tau_{meas}) = b(t, \tau_{meas}) \exp(j2\pi[\phi_{nl}(t - \tau_{ref}) - \phi_{nl}(t - \tau_{meas})]). \quad (20)$$

Table 2. Auxiliary interferometer interpolation

Fiber delay length	0.77 m
Time delay	3.9 ns
Free spectral range	256.5 MHz
Beat frequency at 2000 nm/s	~935 kHz
Equivalent auxiliary sampling rate	~1.87 MHz

Obviously, a perfect correction is only achieved when $\tau_{\text{ref}} = \tau_{\text{meas}}$. In most cases, however, the error can still be significantly reduced for differing delays $\Delta\tau = \tau_{\text{meas}} - \tau_{\text{ref}}$. Assuming a harmonic phase error function $\phi_{\text{nl}}(t) = m \sin(2\pi f_{\text{nl}} t)$ with frequency f_{nl} and modulation index m yields a remaining phase error of the form:

$$\begin{aligned} \phi_{\text{nl}}(t - \tau_{\text{ref}}) - \phi_{\text{nl}}(t - \tau_{\text{meas}}) &= 2m \sin(\pi f_{\text{nl}}(\tau_{\text{meas}} - \tau_{\text{ref}})) \cdot \cos(\pi f_{\text{nl}}(2t - \tau_{\text{ref}} - \tau_{\text{meas}})) \\ &= A_e(\Delta\tau) \cdot m \cos(\pi f_{\text{nl}}(2t - \tau_{\text{ref}} - \tau_{\text{meas}})), \end{aligned} \quad (21)$$

which resembles a phase modulation at frequency f_{nl} with a phase shift that depends on $\Delta\tau$. More importantly, the amplitude is scaled by the factor $A_e(\Delta\tau) = 2 \sin(\pi f_{\text{nl}} \Delta\tau)$, which is smaller than unity when $|f_{\text{nl}} \Delta\tau| < 1/6$. The parameters chosen for the setup (Table 2) yield a beat frequency of ~1 MHz, allowing aliasing-free sampling of sweep-linearity deviation frequency components up to 1 MHz. Suppression of those components would be effective up to a target distance of 25 m in air. Figure 9 compares the measured reflectivity of the anti-reflection coated FC/PC fiber connector at a relative distance of ~2.8 m with and without auxiliary resampling. It can be seen that resampling reduces the peak width by a factor of ~450 while increasing the signal-to-noise ratio by more than 20 dB.

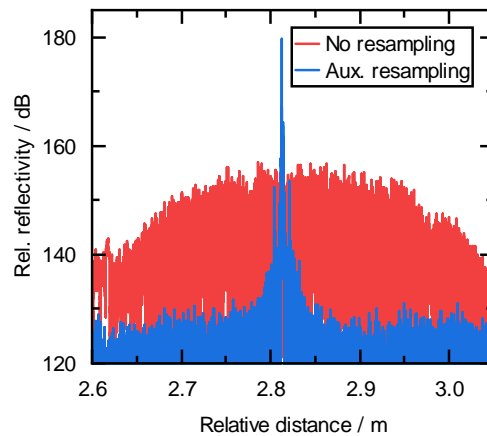


Fig. 9. Comparison of reflection from an anti-reflection-coated FC/PC fiber end when auxiliary resampling is applied (blue) and absent (red).

A.2. Derivation of Eq. (10) and (11)

Starting from the approximation in Eq. (7), the beat frequencies resulting from an up and down frequency ramp are:

$$f_{b,\text{up}}(t) = \frac{2f_{01}v_0}{c} + \frac{2k_1z_0}{c} + \frac{2k_1v_0T_1}{c}, \quad (22)$$

$$f_{b,\text{down}}(t) = \frac{2f_{02}v_0}{c} + \frac{2k_2(z_0 + v_0\Delta t)}{c} + \frac{2k_2v_0T_2}{c}, \quad (23)$$

where f_{01} and f_{02} are the start frequencies, k_1 and k_2 are the sweep rates, and T_1 and T_2 are the durations of the up and down frequency ramps, respectively. Without loss of generality, the down ramp is assumed to start at a time delay Δt after the up ramp. The last term in Eq. (22) and (23) is a frequency offset of $4k_1v_0T_1/2c$ and $4k_2v_0T_2/2c$, respectively, which remains after refocusing the peak to the center of the “blur”. Since the sign of the beat frequency cannot be determined, the sum and difference of the detected peak frequencies are:

$$\Delta_+f_b = |f_{b,\text{up}}| + |f_{b,\text{down}}| = \frac{2f_{01}v_0 + 2k_1z_0 + 2k_1v_0T_1 - 2f_{02}v_0 - 2k_2(v_0\Delta t + z_0) - 2k_2v_0T_2}{c}, \quad (24)$$

$$\Delta_-f_b = |f_{b,\text{up}}| - |f_{b,\text{down}}| = \frac{((2T_2 + 2\Delta t)k_2 + 2T_1k_1 + 2f_{01} + 2f_{02})v_0 + 2z_0(k_1 + k_2)}{c}. \quad (25)$$

Equation (24) and (25) can be combined to determine the position and speed of the target yielding Eq. (10) and (11).

A.3. Effect of intermodal beating on particle speed

Figure 10 plots the measured particle speed close to the input face of the HC-PCF (at 3.568 m). The periodic fluctuations in speed due to intermodal beating are clearly visible. The period of ~ 2.3 mm matches the beat period between the LP₀₁- and LP₀₂-like core modes. The beat pattern decays after ~ 20 cm propagation due to walk-off between the different modal pulses.

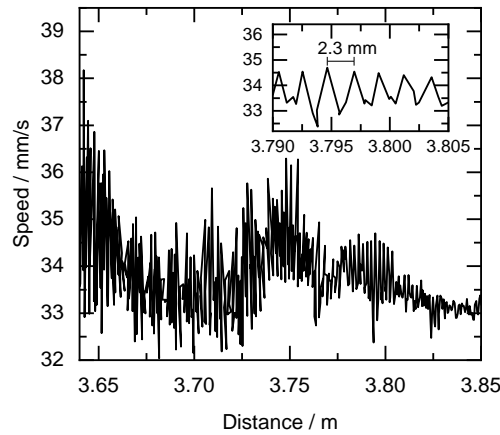


Fig. 10. Periodic oscillation in the instantaneous particle speed observed close to the fiber end face, caused by intermodal beating effect. The inset shows a zoomed-in section where the beat period can be determined.

A.4. Measured particle speed and trapping power fluctuation

Figure 11 depicts the normalized particle speed deviation and the trapping power fluctuation for a ~ 10 s measurement interval. The trapping power propagating towards the PCF was probed with a photodiode placed after a beam splitter while the particle was propelled in the backward direction with an average speed of 32.7 mm/s. It can be seen that the speed variation mostly follows the trapping power fluctuation.

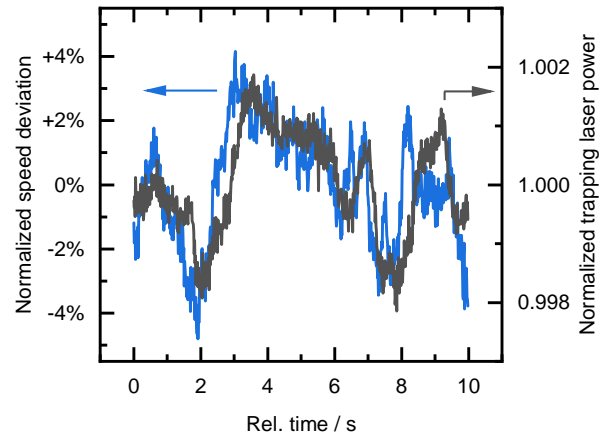


Fig. 11. Measured normalized particle speed and trapping power variation over time.

A.5. Characterization of the speed measurement accuracy

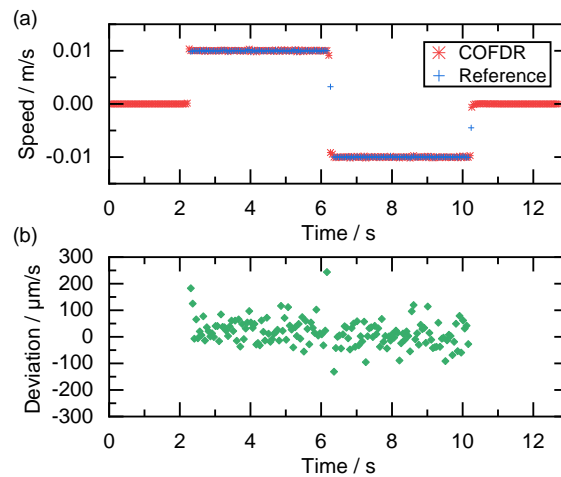


Fig. 12. (a) Moving speed of stage measured by the COFDR system (red) and calculated from the stage trigger signal (blue). (b) Deviation between measured speed and reference (excluding outliers during acceleration/deceleration).

The accuracy of the position and speed measurements was estimated using a gold mirror mounted on a linear stage (Zaber X-LDQ0600C). The stage was set to a speed of ± 10 mm/s. The linear stage outputs a trigger signal every 500 μm as it travels. This was used as a reference.

Aligning the COFDR speed measurements (sweep rate: 2000 nm/s, sweep range: 1518 nm to 1562 nm) with the speed calculated from the trigger signal (see Fig. 12(a)) allowed the deviations to be calculated by linearly interpolating the reference speed at the times when the COFDR measurements were made (see Fig. 12(b)). The standard deviation (excluding outliers during acceleration and deceleration) was estimated as 49.5 $\mu\text{m/s}$. Note that due to limited internal sampling frequency (10 kHz) of the stage, the trigger signal uncertainty is 0.1 ms, causing a speed uncertainty of ~ 20 $\mu\text{m/s}$ in the reference trace.

Funding. Deutsche Forschungsgemeinschaft (418737652); Max-Planck-Gesellschaft; Erlangen Graduate School of Advanced Optical Technologies.

Disclosures. The authors declare no conflicts of interest.

Data availability. Data underlying the results presented here may be obtained from the authors upon reasonable request.

References

1. D. Uttam and B. Culshaw, "Precision time domain reflectometry in optical fiber systems using a frequency modulated continuous wave ranging technique," *J. Lightwave Technol.* **3**(5), 971–977 (1985).
2. W. Eickhoff and R. Ulrich, "Optical frequency domain reflectometry in single-mode fiber," *Appl. Phys. Lett.* **39**(9), 693–695 (1981).
3. R. Passy, N. Gisin, J. P. von der Weid, and H. H. Gilgen, "Experimental and theoretical investigations of coherent OFDR with semiconductor laser sources," *J. Lightwave Technol.* **12**(9), 1622–1630 (1994).
4. U. Glombitza and E. Brinkmeyer, "Coherent frequency-domain reflectometry for characterization of single-mode integrated-optical waveguides," *J. Lightwave Technol.* **11**(8), 1377–1384 (1993).
5. S. A. Kingsley and D. Davies, "OFDR diagnostics for fibre and integrated-optic systems," *Electron. Lett.* **21**(10), 434–435 (1985).
6. B. J. Soller, D. K. Gifford, M. S. Wolfe, and M. E. Froggatt, "High resolution optical frequency domain reflectometry for characterization of components and assemblies," *Opt. Express* **13**(2), 666–674 (2005).
7. J. P. von der Weid, R. Passy, G. Mussi, and N. Gisin, "On the characterization of optical fiber network components with optical frequency domain reflectometry," *J. Lightwave Technol.* **15**(7), 1131–1141 (1997).
8. M. Froggatt and J. Moore, "High-spatial-resolution distributed strain measurement in optical fiber with Rayleigh scatter," *Appl. Opt.* **37**(10), 1735–1740 (1998).
9. S. T. Kreger, D. K. Gifford, M. E. Froggatt, B. J. Soller, and M. S. Wolfe, "High Resolution Distributed Strain or Temperature Measurements in Single- and Multi-Mode Fiber Using Swept-Wavelength Interferometry," in *Optical Fiber Sensors. OSA Technical Digest (CD)* (OSA, 2006), paper ThE42.
10. D. K. Gifford, "Distributed fiber-optic temperature sensing using Rayleigh backscatter," in *31st European Conference on Optical Communication (ECOC 2005)* (IEE, 2005), 511–512 vol. 3.
11. D. Arbel and A. Eyal, "Dynamic optical frequency domain reflectometry," *Opt. Express* **22**(8), 8823–8830 (2014).
12. L. Shiloh and A. Eyal, "Sinusoidal frequency scan OFDR with fast processing algorithm for distributed acoustic sensing," *Opt. Express* **25**(16), 19205–19215 (2017).
13. J. Podschus, M. Koeppel, B. Schmauss, A. Sharma, S. Sundaramahalingam, S. Xie, and P. Russell, "Position Measurement of Multiple Microparticles in Hollow-Core Photonic Crystal Fiber by Coherent Optical Frequency Domain Reflectometry," *27th International Conference on Optical Fibre Sensors (OFS) Alexandria 2021* (2021); accepted for presentation.
14. P. H. Eichel, D. C. Ghiglia, and C. V. Jakowatz, "Speckle processing method for synthetic-aperture-radar phase correction," *Opt. Lett.* **14**(1), 1–3 (1989).
15. D. E. Wahl, P. H. Eichel, D. C. Ghiglia, and C. V. Jakowatz, "Phase gradient autofocus—a robust tool for high resolution SAR phase correction," *IEEE Trans. Aerosp. Electron. Syst.* **30**(3), 827–835 (1994).
16. M. K. Garbos, T. G. Euser, O. A. Schmidt, S. Unterkofler, and P. St. J. Russell, "Doppler velocimetry on microparticles trapped and propelled by laser light in liquid-filled photonic crystal fiber," *Opt. Lett.* **36**(11), 2020–2022 (2011).
17. D. S. Bykov, O. A. Schmidt, T. G. Euser, and P. St. J. Russell, "Flying particle sensors in hollow-core photonic crystal fibre," *Nat. Photonics* **9**(7), 461–465 (2015).
18. D. S. Bykov, S. Xie, R. Zeltner, A. Machnev, G. K. L. Wong, T. G. Euser, and P. St. J. Russell, "Long-range optical trapping and binding of microparticles in hollow-core photonic crystal fibre," *Light: Sci. Appl.* **7**(1), 22 (2018).
19. N. Al Quddus, W. A. Moussa, and S. Bhattacharjee, "Motion of a spherical particle in a cylindrical channel using arbitrary Lagrangian-Eulerian method," *J. Colloid Interface Sci.* **317**(2), 620–630 (2008).
20. W. Sutherland, "LII. The viscosity of gases and molecular force," *The London, Edinburgh, and Dublin Philosophical Magazine and Journal of Science* **36**(223), 507–531 (1893).

21. F. M. White, *Viscous fluid flow*, 2. ed. (McGraw-Hill, 1991).
22. O. A. Schmidt, M. K. Garbos, T. G. Euser, and P. St. J. Russell, "Reconfigurable optothermal microparticle trap in air-filled hollow-core photonic crystal fiber," *Phys. Rev. Lett.* **109**(2), 024502 (2012).